Astron. Astrophys. 329, 276–290 (1998)

ASTRONOMY AND ASTROPHYSICS

Small-scale topology of solar atmosphere dynamics

I. Wave sources and wave diffraction

N.M. Hoekzema[1], **R.J. Rutten**[1], **P.N. Brandt**[2], **and R.A. Shine**[3]

[1] Sterrekundig Instituut, Postbus 80000, 3508 TA Utrecht, The Netherlands
[2] Kiepenheuer-Institut für Sonnenphysik, Schöneckstr. 6, D-79104 Freiburg, Germany
[3] Lockheed-Martin Advanced Technology Center, 91–30/252, 3251 Hanover St., Palo Alto CA 94304, USA

Received 26 May 1997 / Accepted 12 August 1997

Abstract. We study the small-scale topology of dynamical phenomena in the quiet-sun internetwork atmosphere, using short-duration Fourier analysis of high-resolution filtergram sequences to obtain statistical estimates for the co-location probability of different fine-structure elements and wave modes.

In this initial paper we concentrate on the topology of short-duration Fourier amplitude maps for the photosphere and the simultaneously observed overlying chromosphere. We find that these maps portray a complex mix of global modes and locally excited waves which necessitates a statistical approach. Various aspects including mesoscale patterning indicate the presence of subsurface wave sources and of subsurface wave diffraction by convective inhomogeneities.

Key words: Sun: atmosphere – Sun: photosphere – Sun: chromosphere – Sun: granulation – Sun: oscillations

1. Introduction

This paper is the first of a short series on the small-scale topology of the solar atmosphere. Our aim is to study the dynamics of the quiet photosphere and chromosphere in a local approach, searching for links between convective flow patterns and oscillation amplitudes, between photospheric and chromospheric oscillation patterns, and between photospheric and chromospheric fine structure. We do this through statistical analyses of filtergram sequences obtained with the Swedish Vacuum Solar Telescope (SVST; Scharmer et al. 1985) on La Palma.

Rather than isolating a particular one of the various small-scale patterning agents, as is usually achieved by subsonic filtering for convective flow studies and by spatial and temporal averaging for oscillation studies, we study the crosstalk between flows and waves by applying short-duration high-resolution Fourier diagnostics. The technique is introduced here with an initial search for localized sources of photospheric and chromospheric waves.

Send offprint requests to: R.J. Rutten

The present paper and the next one in this series (Hoekzema & Rutten 1997) use cospatial image sequences of the photosphere (G-band filtergrams, called G below) and of the overlying chromosphere (Ca II K_{2V} filtergrams, called K below). We limit the analysis to the quiet-sun internetwork domain, believed to be generally devoid of the kilogauss fluxtubes that make up the magnetic network, and therefore primarily address non-magnetic dynamics.

1.1. Patterning agents

The major patterning agents in the internetwork photosphere and low chromosphere are oscillations and convective flows. The role of the elusive internetwork fields remains unclear. They show up as ubiquitous "pepper-and-salt" bipolar patterns at scales of a few seconds of arc (Livingston & Harvey 1971; cf. Harvey 1977; Zwaan 1987) and with field strengths well below 500 G (Keller et al. 1994). Note that the 500 G value of Lin (1995) describes only the highest peaks, about as rare as internetwork ephemeral regions and the horizontal-field patches of Lites et al. (1996)). The internetwork fields possess a flux distribution that differs intrinsically from the network flux distribution (Wang et al. 1995), indicating that they do not adhere to the evacuated fluxtube paradigm but consist of diffuse field patches that are too weak to act as dynamical patterning agent. They should instead themselves be subject to the convective motions (Zwaan 1987), as indeed observed by Wang et al. (1996) with respect to supergranular flows.

The convective flows on supergranular scales are not addressed here since our high-resolution data cover only a small field at short duration. We therefore concentrate on the granular and mesogranular scales.

The mix of pertinent solar oscillations is impressive. The acoustic wave spectrum alone contains long-period waves, the photospheric five-minute oscillation, the chromospheric three-minute oscillation and (presumably) short-period waves, with further divisions in global and local wave modes as well as propagating, evanescent, standing and shocked waves. In addition,

there are internal gravity waves (e.g., Cram 1978; Damé et al. 1984; Deubner & Fleck 1989; Straus & Bonaccini 1997). In the internetwork areas magnetic wave modes may run along canopies at the chromospheric heights sampled by Ca II K; photospheric internetwork features with relatively large field strength may also take part in chromospheric wave patterning (Brandt et al. 1992, 1994), perhaps through magnetic wave modes (Kalkofen 1996).

1.2. Global and local wave excitation

Our topic of local patterning of photospheric and chromospheric wave amplitudes represents a return to the local emphasis which characterized surface pattern studies of the five-minute oscillation before its global nature was understood (e.g., Musman & Rust 1970; Rice & Gaizauskas 1973). By now, the global p modes represent rather an obstacle to local wave studies, upsetting one-to-one identification of intensity and velocity wave signatures with local pistons. The standard Lighthill-Stein theory of wave excitation by turbulent convection (Lighthill 1952; Stein 1967; cf. Goldreich & Keeley 1977; Goldreich & Kumar 1990; Musielak et al. 1994) assumes a subsonic Kolmogorov turbulence spectrum to predict a generally present acoustic flux spectrum to which localized supersonic flows may add additional wave generation.

Even the p-mode background may be excited intermittently, as proposed by Brown (1991) on the basis of the steep increase of sound generation with turbulence amplitude in the standard theory. This suggestion was taken up observationally by Brown et al. (1992), Goode et al. (1992), Restaino et al. (1993), Rimmele et al. (1995) and Espagnet et al. (1996). The general conclusion from the latter papers is that intergranular lanes, especially long-lived dark features called "intergranular holes" by Roudier et al. (1997), seem to be preferred sites of acoustic wave excitation. This result disagrees with the classical picture in which rising granules are the major pistons for atmospheric wave excitation (Evans & Michard 1962; Meyer & Schmidt 1967; Stix 1970), but agrees with the downflow-driven picture of granulation developed by Rast (1995) in which the "deep fingers" of concentrated subsurface downflows (Stein & Nordlund 1989) are the dominant acoustic sources, in agreement with the p-mode excitation depth estimate of Kumar (1994).

Another local source option is posed by the supersonic outflows at the edges of large granules that occur in numerical granulation simulations (e.g., Cattaneo et al. 1989, 1990; Malagoli et al. 1990) and that may have been observed indirectly by Nesis et al. (1992) or, more convincingly but also indirectly, by Solanki et al. (1996).

1.3. Chromospheric oscillations

At the level of formation of the Ca II K line core, the quiet-sun atmosphere displays a marked split in oscillation patterning between network and internetwork regions. The network elements tend to show long-period intensity modulations, while the internetwork displays the so-called chromospheric three-minute oscillation (e.g., Orrall 1966; Liu & Sheeley 1971; Lites et al. 1993). Movies of Ca II K filtergrams display internetwork emission in spidery, rapidly varying patterns with spatial scales in the 4–10 Mm range. The so-called K_{2V} grains occur as intermittent local brightness enhancements of this pattern, often repetitive with roughly 3-min periodicity and often occurring in close pairs. These have received much attention. The older literature has been reviewed by Rutten & Uitenbroek (1991), more recent work by Rutten (1994, 1995, 1996). The breakthrough K_{2V} grain modeling of Carlsson & Stein (1994, 1997) explains the spectral grain signatures as an acoustic shock phenomenon in which the source function enhancement in weak shocks around h = 1000 km combines with post-shock downfall in higher layers to produce bright emission on the violet side of the Ca II H & K line centers. Their modeling closely reproduces the actual H_{2V} grain evolution patterns observed by Lites et al. (1993) for two out of four cases by emulating the observed underlying photospheric Dopplershifts around h = 260 km with a subsurface piston in a one-dimensional radiative hydrodynamics simulation. Carlsson & Stein's experiments with their piston indicate that a mix of strong 3-min oscillations at h = 260 km with waves of other periodicities, shorter or longer or both, is required to reproduce the observed grain intermittency (Fig. 8 of Carlsson & Stein 1997). The 3-min oscillations alone would create regular grain occurrence by themselves; the other periodicities supply the modulation that cut grain occurrence into the observed patterns. The wave field at h = 260 km so determines the subsequent behavior of the overlying chromosphere in the two successful cases; in particular, K_{2V} grains may develop only where the photosphere supplies sufficient 3-min amplitude (cf. Cheng & Yi 1996; Fig. 1 of Theurer et al. 1997).

How and where the photospheric wave field gets the required 3-min power to produce K_{2V} grains is an open question. Theurer et al. (1997) obtain qualitative reproduction of the observed grain-causing power spectrum from standard turbulent convection modeling after Musielak et al. (1994). Their simulation shows a shift in peak location from the predominantly short-period power excited at $h = -160$ km to 5–3 min periodicities at h = 260 km, a transcription which they attribute to atmospheric response over the travel height. This mechanism would make K_{2V} grain formation ubiquitous over the surface. In contrast, Kalkofen (1996) claims that the grains require localized photospheric events with a location memory for which he invokes internetwork fluxtubes.

1.4. Approach

Case studies in which single events are used to exemplify general patterns in which different agents come together or are even causally related suffer from the confusion that the rich variety of patterning agents and wave modes (not to forget atmospheric seeing) impose on spatially and temporally resolved solar data. Such event studies (e.g., Liu 1974; Cram 1974; Deubner 1975; Cram et al. 1977; Deubner & Laufer 1983; Espagnet et al. 1996; Roudier et al. 1997) tend to give interesting hints of possible mechanisms but do not provide the statistics

needed to estimate their importance or overall role. This is especially the case for spectral data due to their one-dimensional character. On the other hand, Fourier transforms of large-area long-duration data sets reach statistical stability at the cost of mixing diverse regimes (cf. Fig. 5 of Rutten 1994). We therefore combine short-duration Fourier analysis of high-resolution filtergram sequences with small-scale feature separation in an approach which resembles wavelet analysis, but where the data segmentation is fine-tuned to permit recognition of granular fine structure while distinguishing 5-min and 3-min wave modes through Fourier decomposition.

The organization of this paper is as follows. The next section describes the observations. Since the same analysis techniques will also be used on other data in future papers, the reduction procedures in Sect. 3 are given in some detail, in particular the construction of short-duration Fourier maps and the definition of a spatial correspondence factor C to perform selective colocation correlation. Section 4 presents spatial Fourier maps and various measurements without much interpretation, deferring that to the discussion in Sect. 5. We end by suggesting that the presence of localized subsurface wave sources and of subsurface wave diffraction contribute to the topologies of the Fourier maps.

2. Observations

We employ a twin 1.3 h sequence of cospatial and cotemporal photospheric and chromospheric filtergrams of a small quiet region near solar disk center, taken on June 27 1990 with the Swedish Vacuum Solar Telescope (SVST) on La Palma. This day had the best seeing out of a two-week observing run; during 4.5 hours photospheric and chromospheric images were collected in tandem that frequently reached sub-arcsecond resolution. In this paper a subset of 1.3 h duration is used that is most homogeneous in seeing quality. Even then, there were appreciable seeing variations (Fig. 2). The spatial resolution varied between about 0.4 Mm (0.5″) for the best images to about 1 Mm in the fuzziest images retained in this analysis.

The setup at the SVST is shown schematically in Fig. 1. The photospheric images were taken through a 1 nm wide (FWHM) interference filter that transmitted the Fraunhofer G band near λ = 430.8 nm to a COHU video camera. We denote this sequence by G below. The G band contains molecular CH lines that make it a high-contrast diagnostic of the smallest features seen in the photosphere, in particular of the Muller bright points that are thought to mark "fluxtube" sites of strong magnetic fields (e.g., Muller et al. 1989; Muller & Roudier 1992; Berger et al. 1995; Berger & Title 1996). The COHU camera registered frames at video rate of which the best (or at least the better ones) were manually selected in real time for 8-bit digitization and disk storage through grab, hold and choose inspection of a live video display. This (rather exhaustive) procedure resulted in a sequence of 1549 G images taken at somewhat irregular but accurately documented time intervals of about 10 s.

Our G images do not reach the contrast for the tiny (0.2″) intergranular bright points that is seen on newer SVST data

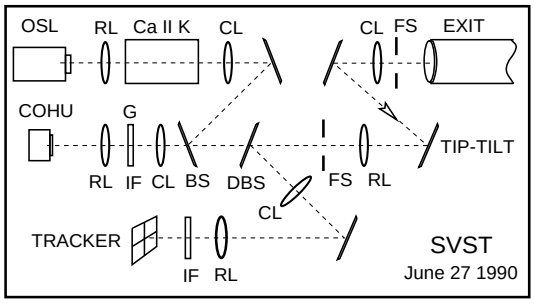

Fig. 1. Sketch of the June 1990 setup on the Lockheed optical table at the Swedish Vacuum Solar Telescope (not to scale). The beam exited from the vacuum refractor through a vacuum window (top right) and was split into three channels by dichroic (DBS) and white-light (BS) beam splitters, to feed *(i)* the prototype digital OSL camera (top left) through the Lockheed Ca II K Lyot filter, *(ii)* a COHU video camera through a G-band interference filter, and *(iii)* a quad-cell sunspot tracker (bottom) which piezo-electrically drove a fast tip-tilt mirror in the primary beam. FS = field stop, CL = collimating lens, RL = reimaging lens, IF = interference filter

with a new 1 nm filter which is more precisely centered on the G band, possibly also because the bright points vanish quickly when the seeing is less than superb (Title & Berger 1996). Nevertheless, our filter imaged the solar granulation sufficiently well to enable separation between granules and intergranular lanes as discussed here, not only during the best seeing but throughout the sequence.

Simultaneously, chromospheric images were digitally recorded on Exabyte cartridges with the Lockheed prototype OSL camera that was used earlier in the Spacelab 2 mission (Title et al. 1989). It was fed through a tunable narrow-band Ca II K Lyot filter that was initially centered at the K_{2V} wavelength but may have slightly drifted off due to temperature changes. These chromospheric images were exposed for 0.4 s at regular intervals of 3.2 s. They cover a much larger field than the G images and have been cropped to the latter. This dataset is denoted by K below.

The passband (FWHM 0.03 nm) of the Ca II K filter was too wide to fully isolate the narrow K_{2V} peaks which the Ca II K profiles show intermittently in the form of the Ca II K_{2V} internetwork grains, so that these filtergrams do not show the high K_{2V} grain intensities that are displayed in high-resolution Ca II H & K spectrograms (e.g., Cram & Damé 1983; Lites et al. 1993; Hofmann et al. 1996). Our K images nevertheless display, at lower modulation, the internetwork dynamics patterns to which the K_{2V} grains belong, because wider-band registration than the spectral width of the K_{2V} feature does not produce significant differences in the resulting spatio-temporal patterning. This is demonstrated by Fig. 2 of Rutten (1994), which shows only small modulation amplitude differences and small phase differences between narrow-band H_{2V} and wider-band H-core time slices constructed from the spectra of Lites et al. (1993).

A small sunspot was selected as target for the Lockheed high-speed image tracker system. It used quad-cell centering

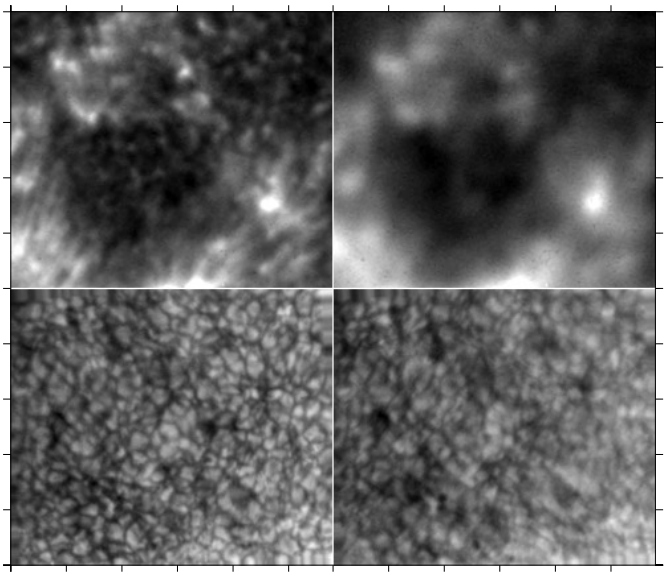

Fig. 2. Two K and G pairs of sample images taken during good seeing (left) and bad seeing (right). The field size is 29×25 Mm^2 (41×36 arcsec^2); the tick marks are at 5 Mm spacing. Top: Ca II K frames (K) taken at 10:40:03 UT and 10:39:15 UT. The brightest patches outline the chromospheric network. It encompasses an internetwork "cell" in which small grey features correspond to the Ca II K_{2V} grains observed with narrower bandpass. Some "measles" are present in the form of dark pixels but are evident only at large magnification. Bottom: cospatial and nearly cotemporal G-band granulation frames (G). The degradation from good to bad seeing is worse for K than for G due to longer exposure, but the intrinsic scales in K images are also larger than in G images. The elongated granules at bottom right in the G images are artifacts introduced by the correction for field rotation and are excluded. The righthand images were discarded in the analysis

of a pick-off image in the red to feed correction signals to a high-speed tip-tilt mirror placed before prime focus. The spot is present in the large field of the K images but not in the smaller field covered by the G images, for which a fairly quiet region was selected away from the spot. This subfield is shown in Figs. 2–3. In the K images, fairly bright network surrounds a network cell with a diameter of about 15 Mm. Another quiet area covers the upper right corner. The G images show regular granulation over the full frame. The network does not contain sufficient strong-field concentrations to disturb the convection into the abnormal granulation patterning that is evident in plage (Title et al. 1992).

Previous analyses of these data have been reported by Brandt et al. (1992, 1994). These concerned a "persistent flasher" seen in the K movie that accurately tracks the photospheric flows derived from the G movie, and the lifetime of the mesoscale flow patterns measured from the photospheric flows.

3. Reduction

Field corrections. The data reduction started with dark field subtraction and flat field normalization. The G sequence was corrected for the geometrical rubber-sheet distortions caused by the seeing on scales larger than granules with the Lockheed "destretching" software using local correlation tracking (Title et al. 1989, cf. Strous 1994 p. 35 ff). The K images were not corrected, but due to their much longer exposure time these represent geometrical averages in themselves. Careful co-alignment of the G and K sequences was established from calibration images taken through a fine-scale geometrical grid pattern. The remaining field rotation was corrected for both sequences, causing the artificially elongated granules at bottom right in the G panels of Fig. 2. They are excluded from the analysis.

The area of the K field covered by the G field was resampled on the same scale, resulting in a double sequence of cospatial G and K images with a field size of 29 Mm by 25 Mm at 0.12 Mm pixel size, not exactly synchronous but with image pairs taken close enough in time to permit correlation of events and structures in the chromosphere with events and structures in the underlying photosphere.

Data selection. The present paper is limited to a 1.3 hour subset taken during 10.39–11.55 UT, chosen because the seeing was most homogeneous and the image rotation (due to the SVST alt-azimuth mirror configuration) the smallest. Sample images are shown in Fig. 2, where we have chosen not only to display "typical examples" of good quality but also bad quality ones. The K images are always fuzzier than the G images, not only because the K exposure times were much longer but also because the chromosphere as seen in the K line is intrinsically less detailed due to the strong resonance scattering in this line, effectively smearing fine structure to about 1 Mm (cf. Owocki & Auer 1980). The degradation from good to bad seeing is worse for K than for G, but the intrinsic difference in structure scales makes the effect of the seeing variations similar for both. Even in the bad frames, G granules and K brightenings are still recognized.

The next step was to compute a one-dimensional spatial power spectrum per K image and to use that to diagnose the occurrence of "measles" in the K frames. These are individual pixels that are momentarily exceptionally bright or dark in individual frames from the OSL camera due to unidentified noise sources. Frames with an overdose of measles stand out in their spatial power behavior because the one-pixel spikes produce large power at the highest spatial wavenumbers. About twenty frames in the K sequence were found to be contaminated so badly that they have been rejected. Median filtering was used to remove the remaining measles from other K frames.

Similarly, the spatial power at wavelengths between 1.5 and 3 Mm was used as criterion to select the sharpest G and K images. This spatial frequency band supplies a good indicator of seeing quality, with larger power invariably corresponding to sharper images (Strous 1994 p. 43). The 1.3 h sequences were divided into 228 bins of 20 s; for each bin, the better half of the images taken in that period were averaged to provide a single reference image. For the G data, a few bins did not contain images; these gaps were filled through interpolation. The result consists of two cospatial and cotemporal G and K data cubes,

each containing 228 images at 20 s separation spanning 75 min. These two cubes form our input data.

Fourier maps. We have constructed short-duration Fourier amplitude maps per pixel from the G and K cubes in the following manner. For each location in the field, ten partially overlapping brightness histories were extracted from each cube. These segments are 22 min long but were apodized with a cosine window function that enhances the modulation by a factor two at the center of a segment and reduces it to zero at the ends, and reduces the 22-min duration to an effective value of about 15 min. Each segment was then Fourier transformed to provide a short-duration modulation spectrum per pixel in which edge effects are suppressed by the apodization. Examples of the resulting Fourier amplitude maps are shown in Fig. 6.

The effective duration of 15 min was chosen as the maximum over which G images may be averaged without too much loss of granular patterning, while still permitting frequency resolution between 5 min and 3 min periodicity. The granulation pattern indeed survives temporal averaging over this duration (Fig. 3), even though many individual granules live shorter. In fact, granular patterning remains present at low contrast after averaging over a full hour. Our 15 min averaging enhances the weight of relatively long-lived and relatively stationary features.

The successive brightness histories per location are stepped by 5 min differences in starting time. We used ten of them, ignoring the last 9 min of the data cubes which are spoiled more frequently by bad images. Therefore, the brightness histories together span a total duration of 60 min in effective extent. Their Fourier transforms show power evolution in 5-min steps. Since successive spectra are derived from two-thirds overlapping histories, only the transforms that are separated by more than 20 minutes in their moment of mid-point sampling refer to fully independent data. Rather than obtaining transforms of the brightness modulation of each individual image pixel, boxcar averaging was first applied over 3 by 3 pixels to both sequences. This spatial smoothing reduces the noise appreciably. Its effect on the spatial power patterning is small since the intrinsic resolution of most images is worse than 3 pixels or 0.36 Mm (the SVST diffraction limit is at 0.16 Mm). A test using 5 by 5 pixel averaging produced Fourier maps with only slightly less detail.

Brightness distinctions. In order to enable comparisons between Fourier amplitude and atmospheric morphology, we have split the observed field into fine-structure components using the temporally averaged brightness as criterion for both G and K. In this procedure we did not normalize spatial variations to the average brightness of the whole field because there are non-solar gradients across the images (for example a brightening from left to right in the G panel of Fig. 3) as well as large-scale solar fluctuations due to the five-minute oscillation. We therefore assign pixels to brightness classes by comparing their brightness value to the local mean brightness obtained from boxcar averaging over smaller subfields. The subfield sizes were defined by trial-and-error tests in which the patterns that result after subtraction of the locally-normalized average were compared with the input data. For the G data the selected subfield size is 1.7×1.7 Mm^2 (14×14 pixels); for the K data we use 18×18 Mm^2 (150×150 pixels). Examples of this local normalization are shown at right in Fig. 3.

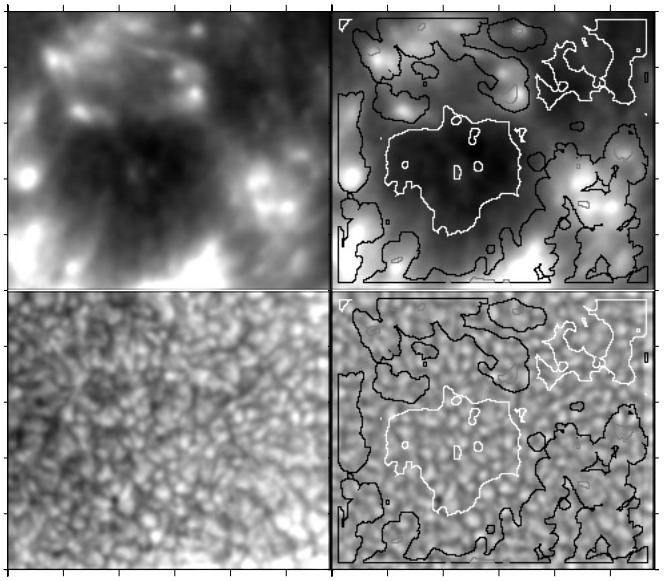

Fig. 3. Left: time-averaged K and G images. Tick marks at 5 Mm intervals. The apodization of the two 22 min sequences results in effective brightness averaging over about 15 min. Granulation is still visible (G, lower panel); the chromospheric network is enhanced with respect to instantaneous images (K, upper panel). Right: locally-normalized K and G averages with overlaid black and white contours. The latter were determined from the average brightness of the complete 50-min K sequence and divide the field into network (bright areas within black contours), internetwork (dark areas within white contours) and an intermediate brightness regime that is excluded from both. The edges of the field are excluded as well

Pixels in the 15-min G sequence averages that are brighter than the local average are called "granules", while the subset with brightness over 110% are defined to be "bright granules'. Similarly, "intergranular lanes" are less bright than the local average, while "dark lanes" are below 90%. The dark lanes occupy about 10% of the total area, lanes 53%, granules 47% and bright granules 8%. In the K data, a similar distinction is made in order to separate network and internetwork. Pixels that have time-averaged brightness larger than 130% of the local average in any of the ten 15-min averages are defined to be "network", while the "internetwork" is defined as the pixels with average brightness below 70% in all ten 15-min averages. The asymmetry is introduced in order to identify internetwork conservatively; for the same reason, the large intermediate region is not counted as either. A network criterion similar to the internetwork one, requiring pixels to be brighter than 130% of the average in all ten 15-min averages, produces only a few tiny, isolated peaks. These are specified by grey contours within the bright areas in Fig. 3. The area fractions are 0.6% for these net-

work peaks, 31% for network, 18% for internetwork and 51% for intermediate brightness.

The network/internetwork distinction is illustrated at right in Fig. 3 by contours overlaid on one pair of locally normalized 15-min averages. The small contours inside the dark internetwork areas mark locations that were bright only briefly during the one-hour sequence. They were not included as internetwork because their brightening may be of network-like magnetic origin, comparable to the persistent flasher that occurred earlier in the K image sequence taken that day (Brandt et al. 1992, 1994). From watching the K movie we think it more likely that these temporary brightenings mark normal K_{2V} grain activity of acoustic origin, not differing significantly in its surface patterning from the remainder of the internetwork, but we prefer to restrict our designation of the latter conservatively to the locations with darkest average K brightness in order to exclude all potential strong-field sites.

Co-location probability. The last item of this section concerns a statistical quantity C which we call "spatial correspondence" and which we use in Figs. 9–10 below and in forthcoming papers to measure morphological alignments between images and maps such as Fourier amplitude charts. It specifies the normalized fractional cospatiality of two pixel classes between different images or maps, representing selective spatial correlation that is restricted to areas of given morphology and is not weighted by amplitude. Formally, the spatial correspondence is defined by

$$C \equiv \frac{f_{\rm AB}}{f_{\rm B}} = \frac{N_{\rm AB}/N_{\rm A}}{N_{\rm B}/N}, \qquad (1)$$

where the coincidence filling factor $f_{\rm AB} = N_{\rm AB}/N_{\rm A}$ specifies the fraction of pixels of type A in one image or map covering the observed field (or a specified subfield such as the internetwork area in this paper) that also belong to type B in another image or map covering the same field, and where the filling factor $f_{\rm B} = N_{\rm B}/N$ measures the spatial occurrence of the second category in the (sub-)field. By normalizing $f_{\rm AB}$ by $f_{\rm B}$ the spatial correspondence C quantifies the likelihood that the two types of behavior are cospatial on a probability scale where $C = 1$ suggests that A and B are independent phenomena. Values $C > 1$ imply that pixels of type A are preferentially co-located with pixels of type B, whereas values $C < 1$ imply spatial avoidance. Thus, C specifies the co-location probability in terms of the random-draw likelihood. Its value does not change when exchanging A and B.

For example, let A be a G image, let B be another G image taken only 20 sec later, and let C express granule co-location. Since 98% of all pixels that belong to the granule class in A are still granule in B, the granule coincidence fraction is $f_{\rm AB} = 0.98$, and since the granule pixels have filling factor $f_{\rm B} = 0.47$, the granule-to-granule correspondence between the two images is $C(\Delta t{=}20\,{\rm s}) = 0.98/0.47 = 2.1$. It expresses that granule pixels have twice the random-draw likelihood to be granule again, i.e., that granules live longer than 20 seconds. The same may be done for the bright-granule pixels in the two images. About 56% of these still belong to the bright-granule class after 20 s so that their spatial correspondence is $C(\Delta t = 20\,{\rm s}) = 0.56/0.08 = 7.0$. If pixel brightness was a random draw after 20 s, only 8% of the bright pixels would again qualify as bright. The seven times larger co-location probability expresses that exceptionally bright pixels lie preferentially in the center of well-developed granules that do not vanish within 20 s.

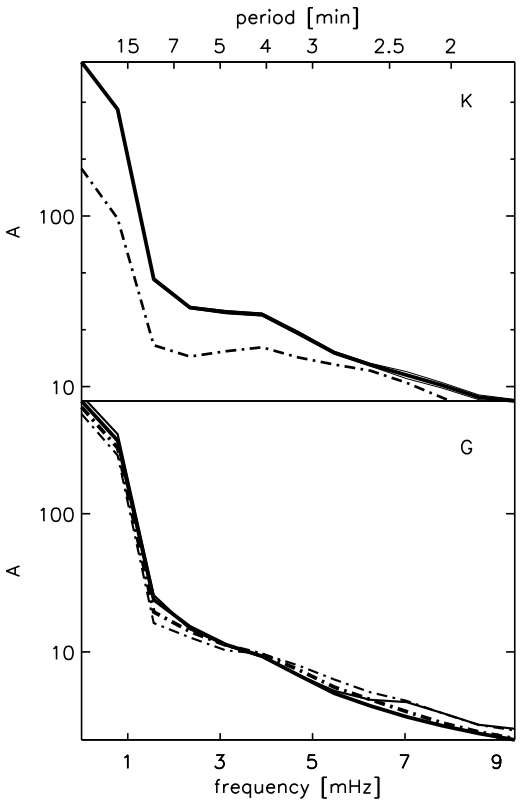

Fig. 4. Selectively averaged temporal Fourier spectra. The Fourier amplitude A (square root of the power, in arbitrary units on a logarithmic scale) of the observed temporal brightness variations is averaged over all pixels of a given type and plotted against temporal frequency f (bottom axis) and corresponding period P (top). Each curve is the mean from ten overlapping data sequences with effective durations of 15 min. Upper panel: K data, split between network (solid curve) and internetwork (dot-dashed). The internetwork has smaller power at low frequencies. Lower panel: G data, internetwork pixels only, split between granules (thick solid), the brightest granules (thin solid), intergranular lanes (thick dot-dashed) and the darkest intergranular areas (thin dot-dashed). The slight differences between these curves are enhanced in Fig. 5

The advantages of this statistical measure are that it may be estimated reliably from sufficiently large data sets even for pixel classes with small filling factor and that it compares relative surface patterning without sensitivity to the magnitude of a phenomenon within the given type. It serves to establish spatial co-alignment of different phenomena in the presence of many different patterning agents and without sensitivity to the response magnitude at which such spatio-temporal pattern coupling may occur.

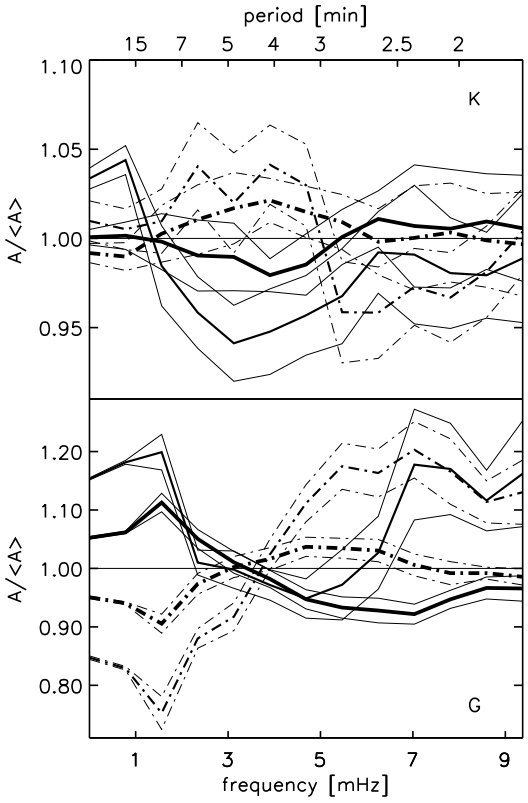

Fig. 5. Differential K and G Fourier spectra, split between granules and intergranular lanes in internetwork areas. Ordinates: normalized Fourier amplitude $A/<A>$ with $<A>$ the average amplitude for the whole internetwork area. Abscissae: temporal frequency (bottom) and corresponding period (top). The spatial averaging is split between granules (thick solid curves), the brightest granules (thin solid), intergranular lanes (thick dot-dashed) and the darkest intergranular areas (thin dot-dashed) for both the K data (upper panel) and the G data (lower panel). Each curve is the average of ten 15-min segments; the thin curves show corresponding one-sigma rms estimates. The lower panel is an enhanced display of the relative differences between the curves in the lower panel of Fig. 4

4. Results

4.1. Temporal Fourier characteristics

Fig. 4 shows temporal Fourier spectra determined from the K data (upper panel) and G data (lower panel). Each curve is the average over all pixels of the specified category over the ten data sequences. The low-frequency limits represent the time-averaged contrast between the pixel categories.

The network and internetwork Ca II K curves in the upper panel represent characteristic power behavior that is also displayed in Fig. 1 of Cram (1978); Fig. 4 of Kulaczewski (1992); Fig. 5 of Lites et al. (1993); Fig. 7 of Steffens et al. (1995) and Figs. 5 and 7 of von Uexküll & Kneer (1995). There are differences in frequency resolution (which is low here), in normalization (the average intensity is subtracted in some papers so that the power is zero at $f = 0$) and in regime separation (no network/internetwork split in some papers), but the overall behavior is as shown here: low-frequency power dominates in network elements while internetwork regions gain relative power in the $f = 3 - 7$ mHz band which contains the so-called three-minute chromospheric oscillation. However, this increase is much smaller than the $f = 3 - 7$ mHz signal which the chromospheric oscillation produces in Ca II K_3 Dopplershift; the oscillation is primarily a Doppler phenomenon (e.g., Noyes 1967; Cram 1978; cf. Rutten 1995). The corresponding intensity modulation gains amplitude when the passband is limited to the much narrower K_{2V} feature as shown in the passband comparisons in Fig. 2 of Rutten (1994), but the surface patterns of the chromospheric oscillation are the same in the wider passband used here (same figure).

The lower panel shows only slight differences between the different pixel classes. Nevertheless, these are significant. This becomes evident after normalization by the average Fourier amplitude per frequency bin in Fig. 5. Its lower panel displays the same differences at a magnified scale. The ordering at the left-hand side of the plot again represents the time averages per pixel class. It illustrates the split into bright granules, granules, lanes and dark lanes defined above. For increasing frequency the curves in the lower panel initially rise and drop, respectively, to peaks corresponding to granular lifetimes. The curves then come together in the five-minute band around $f = 3$ mHz, illustrating that the photospheric five-minute oscillations are primarily global and rather insensitive to the local fine structure. Around the acoustic cutoff frequency ($f = 5.5$ mHz) the dark-lane curve rises steeply to high values, significantly above average. This rise indicates that the darkest intergranular lanes coincide spatially with larger than average acoustic power in the three-minute regime. At the righthand side of the lower panel, the brightest granules and the darkest lanes show similar excess of power over the average value. We suspect that this is partially due to seeing excursions. The apparent jitter of small features around their intrinsic location produces high-frequency modulation at relatively large amplitude when the features have large contrast (Endler & Deubner 1983).

The upper panel of Fig. 5 again shows chromospheric K amplitude spectra, but now only for the internetwork areas and split between the granular features measured in the G band for the underlying photosphere, just as in the lower panel. Over the $f = 2 - 5$ mHz range there is an appreciable split between small K amplitudes above bright granules and large K amplitudes above dark intergranular lanes. In addition, the latter curve shows a strikingly steep drop around $f = 5$ mHz. Although the error bands are wide, these features seem significant, the more so because the thicker curves for smaller granular contrast show a similar split at smaller amplitude. We interpret the pattern in terms of diffraction in Sect. 5, but first add more evidence.

4.2. Spatial Fourier characteristics

Fourier maps. Figs. 6 and 7 display spatial Fourier amplitude maps with variation in grey scale encoding. In these figures the Fourier amplitude A per pixel that has been computed from one pair of 15-min G and K sequences (the same pair as in Fig. 3)

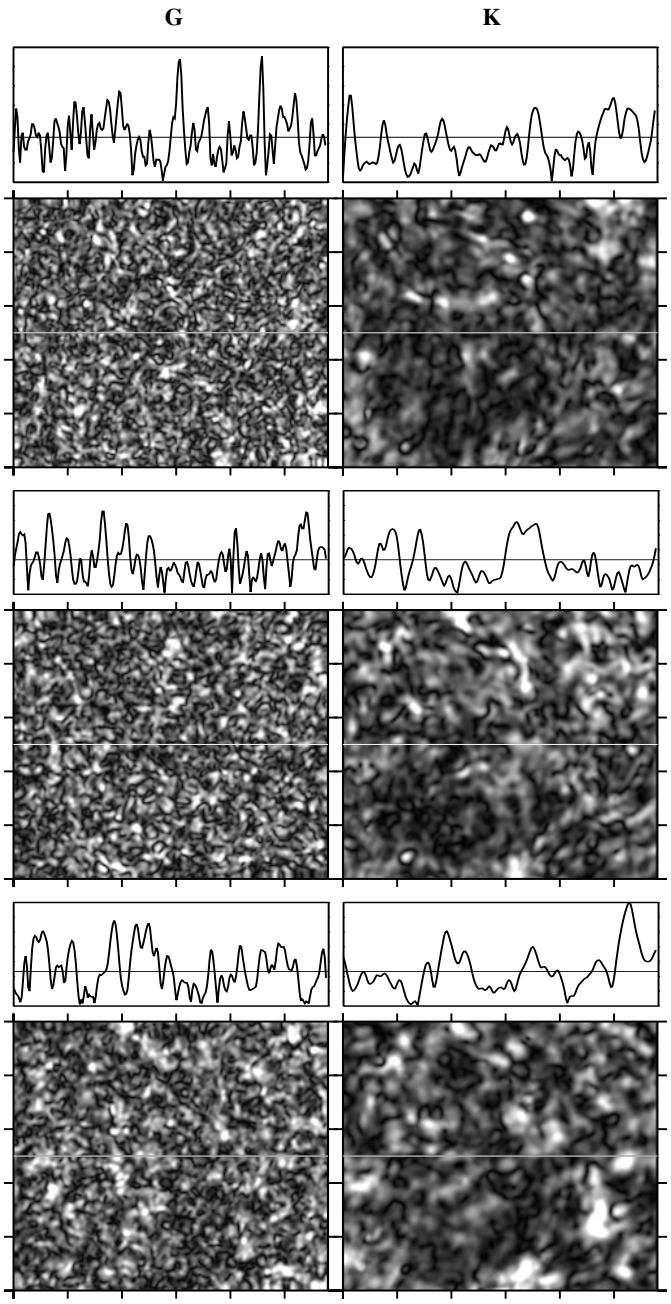

Fig. 6. Fourier amplitude maps from G (left) and K (right) filtergrams. The ticks are at 5 Mm spacing. The grey scale displays Fourier amplitude A per pixel measured over 15 min effective duration in three 1.5 mHz wide bands centered on f = 7.8 mHz (2 min periodicity, top), f = 5.5 mHz (3 min periodicity, middle) and f = 3.1 mHz (5 min periodicity, bottom). The tracing above each map shows the variation of A along the horizontal cut marked by the white line across the map. These Fourier maps show much fine structure of which the characteristic scales increase both with height in the atmosphere (from G to K, left to right) and with periodicity (from top to bottom). The chromospheric network is vaguely outlined by the brightest patches in the 5-min K map (bottom right, compare with Fig. 3). The morphological difference between high and low amplitude areas is emphasized in Fig. 7

is split between separate charts mapping the 2, 3, and 5-min contributions.

The maps in Fig. 6 have linear grey scale coding; the tracings above each panel show the variation of A along the cuts marked by white lines on linear scales. The K maps in the right-hand column are similar to the power maps in Fig. 3 of Damé et al. (1984) and similarly show that oscillatory power tends to be concentrated in small point-like areas with erratic patterning. The network is evident only in the 5-min panel at bottom right. At higher temporal frequency the morphology has smaller scales. Similar behavior is seen in the G amplitude maps on the left. These are comparable to the lower-resolution velocity power maps of Brown et al. (1992). The G amplitude patterning is also spatially intermittent, with characteristic scales that are considerably smaller than for the K maps but that decrease similarly with increasing temporal frequency. Apart from the scale differences, the G and K amplitude distributions are more alike in their morphology than the original images (Fig. 2). The tracings show large amplitude excursions, in each case ranging from $A \approx 0$ to twice the average values marked by the horizontal lines.

The maps in Fig. 7 display the same A values on a logarithmic scale (left) and with coarse binning (right). These grey scale choices emphasize the spatial morphology difference between the occurrence of the largest Fourier amplitudes and the occurrence of the smallest Fourier amplitudes. There is a striking split between these at each of the three periodicities. The bright locations of large Fourier amplitude tend to show up as isolated, roundish peaks or as conglomerates of peaks, whereas the dark low-amplitude locations tend to make up slender and elongated areas, more like wiggly snaking worms than roundish patches. The 5-min K maps show some elongated bright patches too, but those are in the network areas and represent network outlines.

Spatial decomposition. The spatial structure of these temporal Fourier maps is decomposed into spatial Fourier components in Fig. 8. Each of the G and K Fourier amplitude maps was apodized with a cosine bell function. Their two-dimensional spatial transforms were converted into one-dimensional wavenumber spectra by annular averaging. The ten spatial wavenumber spectra that so resulted per 2, 3 and 5-min periodicity in G and K were averaged to produce the curves and error bounds in Fig. 8. The solid curves are similar spatial decompositions of the 15-min averaged images shown in Fig. 3, on scales that are reduced by a factor ten; the latter corresponds to the low-frequency amplitude drop in Fig. 4. For the K data this curve peaks at the largest scales, representing the stable structuring of the chromosphere into network and internetwork regions. The solid curve for the G average peaks at spatial wavelengths $\Lambda = 1.2 - 4$ Mm, corresponding to the granulation and the interference patterns of the five-minute oscillation.

The amplitudes shown by the other curves are larger for longer periodicity in both panels, conform Fig. 4. The curves drop much less steeply with wavenumber for G than for K, a difference to which seeing jitter may contribute. The lower-panel dot-dashed curve which describes the spatial wavelengths of the 5-min G maps peaks at Λ = 1.9 Mm; there is a similar peak at that wavelength in the 5-min K curve (upper panel). This

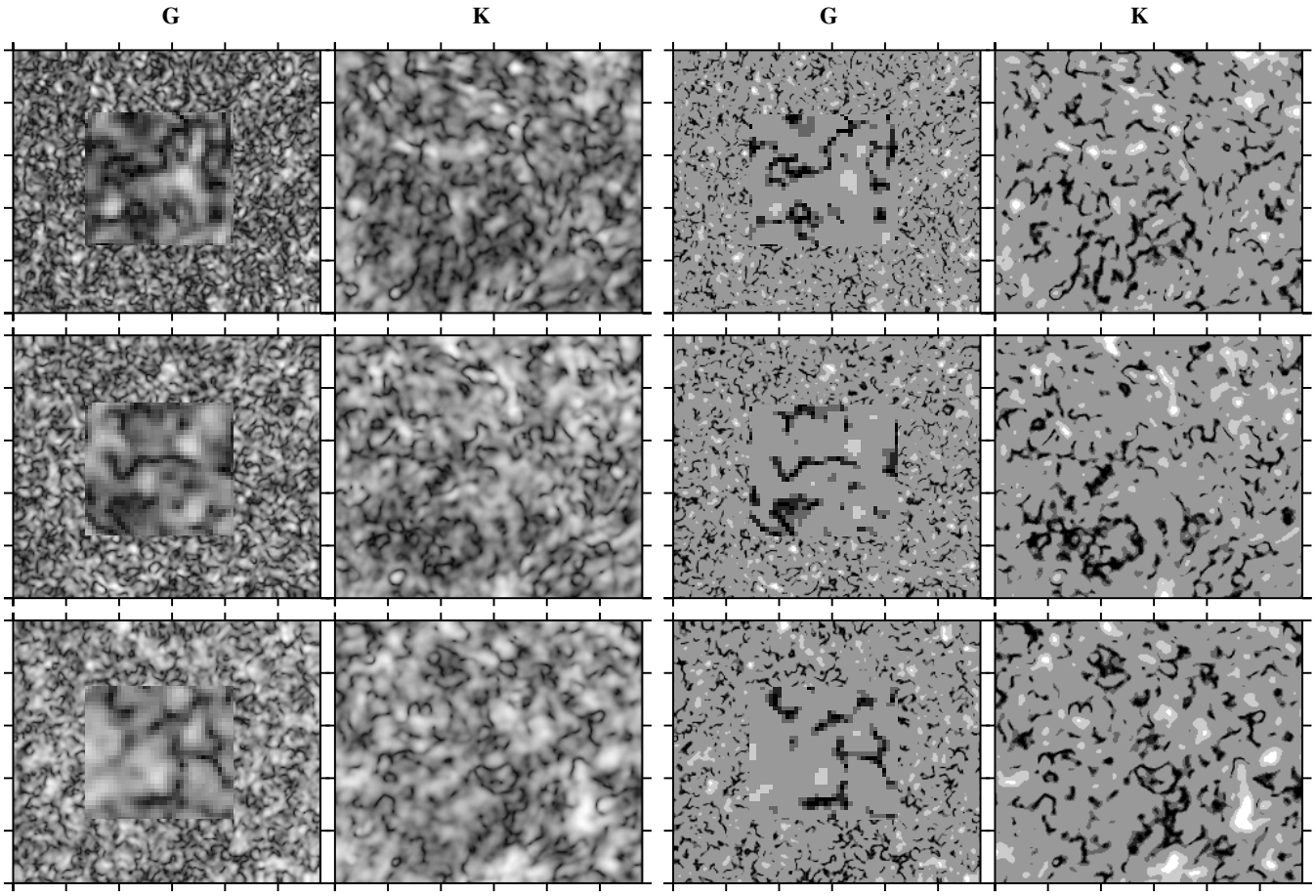

Fig. 7. Fourier amplitude maps as in Fig. 6, but with different grey scaling. The G panels contain insets which are enlargements (at three times linear magnification) of their central parts. Lefthand G and K columns: the grey scale displays log A. Righthand G and K columns: coarse amplitude binning in which the black areas have A below 20% of the map average and the other shades (dark grey to white) correspond to $20-33\%$, $33-50\%$, $50-200\%$, $200-300\%$ and over 300% of the map average, respectively. The $50-200\%$ bin makes up the background. These displays illustrate that large-A areas (white) in the internetwork regions tend to be roundish, whereas low–A regions (black) tend to have rope-like appearance

wavelength corresponds to the 5-min location of the f-mode in a $f-k_h$ diagram. The peak may betray the presence of the $f-k_h$ ridge that would be resolved using longer-duration data sequences covering a larger field. The hump in the 5-min curves at longer wavelength may similarly reflect p_1 and higher-order p-modes at low resolution and contrast.

The two sets of three curves confirm the topological similarities and scale changes in Fig. 6. As disparate as the photospheric G and chromospheric K images themselves are, their Fourier maps are build up from comparable components with gradual shifts of emphasis rather than striking differences between them. The characteristic wavelengths are smaller for G than for K; they diminish with decreasing periodicity for both G and K. Note that the short-period contribution is larger, relative to the 5-min one, for K than for G. In particular, the 3-min contribution to the K maps nearly equals the 5-min contribution in the $\Lambda = 1-1.5$ Mm regime of the Ca II K grains. (It would be much larger if the maps charted K_3 Dopplershift or narrow-band K_{2V}/K_{2R} modulation for the internetwork only.)

4.3. Fourier crosstalk

The statistical correspondence C defined by (1) is used in Fig. 9 to study co-location of the amplitude patterns in simultaneous Fourier maps for different periodicities. Such alignments indicate the amount of crosstalk between different frequencies. Only the internetwork areas outlined in Fig. 3 are taken into account. The curves are again averages over the ten different (partially overlapping) pairs of image sequences, with corresponding error estimates. The top and bottom panels of Fig. 9 display crosstalk between Fourier maps of different temporal frequencies that are derived from the same image sequence, respectively comparing K with K and G with G. The various curves specify the average co-location probability for larger-than-average amplitude pixels per 2, 3 or 5-min map with the same pixels in maps for all other frequencies from the same data. Each curve has an auto-correspondence peak of $C \approx 2$ at its own frequency. The large width of these peaks reflects the low frequency resolution that results from the 22-min data string lengths. There is no crosstalk

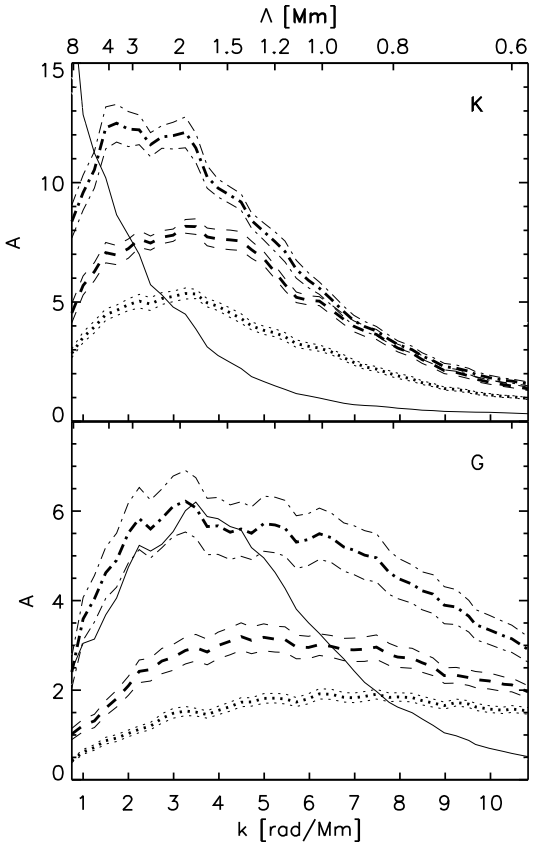

Fig. 8. Spatial Fourier analysis of temporal Fourier amplitude maps as in Fig. 6, respectively for K filtergrams (upper panel) and G filtergrams (lower panel). Abscissae: spatial wavenumber k (bottom) and corresponding wavelength Λ (top). Ordinates: Fourier amplitude A per wavenumber bin, in arbitrary units and without distinction between network and internetwork. Each curve shows the average wavenumber spectrum obtained from 10 apodized Fourier amplitude maps, with corresponding rms error estimates. Dash-dotted curves (reaching highest): wavenumber spectra measured from the 5-min Fourier maps. Dashed curves: same from 3-min maps. Dotted curves (lowest): same from 2-min maps. The solid curves are comparable spatial Fourier spectra obtained from the 10 locally normalized 15-min K and G image averages (such as the ones shown at right in Fig. 3) on a ten times compressed scale

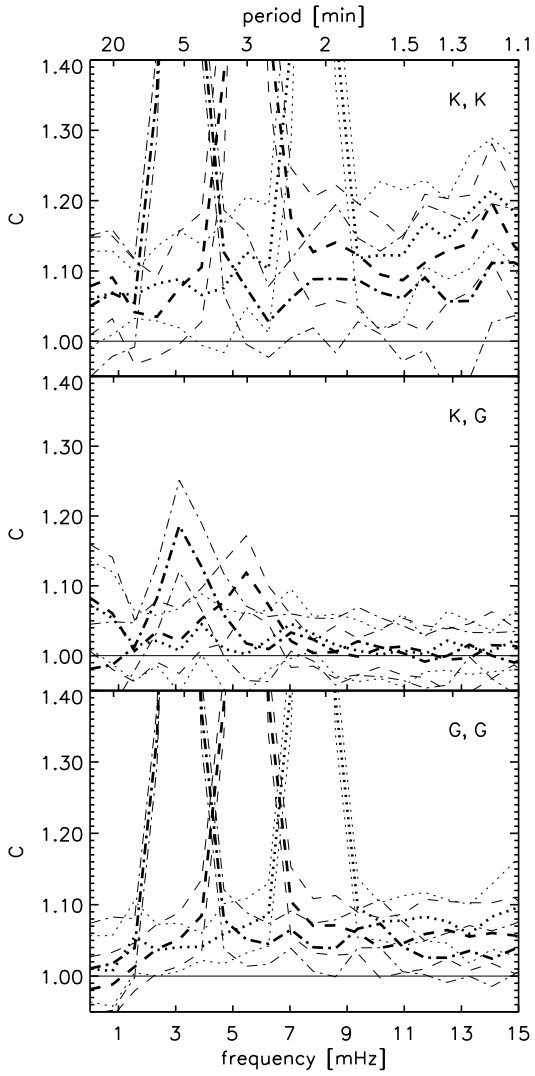

Fig. 9. Fourier crosstalk, measured by the spatial correspondence $C(f)$ for internetwork pixels with larger-than-average Fourier amplitude between simultaneous Fourier amplitude maps of different periodicity. The value $C = 1$ implies that above-average pixels in one map do not favor the location of large-amplitude pixels in the other map while values $C > 1$ imply preferential co-location. Top panel: K maps compared with K maps. Middle panel: K maps compared with G maps. Bottom panel: G maps compared with G maps. Dash-dotted: large-amplitude correspondence between 5-min Fourier maps and simultaneous maps of the frequency/periodicity specified along the horizontal axes. Dashed: same for 3-min maps. Dotted: same for 2-min maps. The thin curves specify one-sigma rms variations. Without crosstalk between frequencies, each curve would peak at its own frequency value and have $C = 1.00$ elsewhere. The crosstalk is larger in K_{2V} than in the G band. The 5-min and 3-min peaks between G and K are very low

between different frequencies when $C \approx 1$ outside the peaks. This value is reached at left in the bottom panel, implying that the bright elements of the time-averaged G images (i.e., granules) play no significant role in governing the simultaneous photospheric oscillation amplitude patterns at any frequency. There is some crosstalk between frequencies elsewhere in the bottom panel. It may again result from seeing jitter of small granular structures with large contrast, a broad-band phenomenon that may contribute some modulation at most frequencies.

In the upper panel of Fig. 9 the (K, K) C-values are larger outside the peaks and seem to increase with frequency. We believe these to be significant because seeing jitter affects the K sequences less than the G images. It may be due to the sawtooth waveforms that are produced by chromospheric shocks.

The middle panel of Fig. 9 measures the spatial correspondence of Fourier amplitude patterns as displayed in Fig. 6 between photosphere (G) and chromosphere (K). The 5-min and 3-min curves show peaks that seem significant but have low amplitude. If these modulations of the photospheric and the chro-

mospheric brightness are both set by global mode interference patterning, one would expect peaks near the 100% correspondence value $C \approx 2$. For the five-minute oscillation the waves are evanescent so that such cospatiality should be instantaneous, but also waves that travel from the photosphere up to the chromosphere (taking two to three minutes at sound speed) contribute to such a peak within the 15-min duration of the data strings. The low peak values therefore confirm the considerable deviation from vertical correspondence exhibited by Fig. 6 even for the patterning agents that should correlate best.

4.4. Fourier persistence

The next issue concerns the temporal stability of the spatial patterns in Fourier maps. Their time evolution is studied in Fig. 10. In this case, the spatial correspondence is measured between Fourier maps constructed from sequences at different time lags for pixels that have above-average Fourier amplitude. This is again done for the internetwork areas marked in Fig. 3 only.

The bottom panel shows the persistence of the G amplitudes. All three curves, for 5, 3 and 2-min periodicity respectively, drop steeply down at a time delay $\Delta t \approx 10$ min, to reach $C \approx 1$ at $\Delta t = 15$ min. At $\Delta t = 0$ min the 1:1 correspondence produces $C \approx 2$, but since the 15-min time histories from which successive maps are constructed overlap partially in 5-min steps, this auto-correspondence extends to $\Delta t = 10$ min. The fact that it vanishes around $\Delta t = 15$ min confirms that our choice for the history durations is a good one, in the sense that the photospheric Fourier morphology does not live longer.

The persistence of the K maps in the top panel shows rather different characteristics. There is a similar decay of C near $\Delta t = 10$ min, but in this case it is followed by significant excess above $C = 1$ out to $\Delta t = 35$ min, especially for the 3-min maps. This behavior indicates that the dynamical patterns in the chromosphere possess a partial location memory over longer time scales. Such behavior is to be expected for the bright elements that outline the Ca II network, possessing spatial memories due to the concentrations of magnetic flux which they represent. However, the curves in Fig. 10 are from internetwork areas only, excluding even the areas that are only momentarily bright and may represent loose patches of field (Sect. 2). The global p-modes also possess long memories individually (or they wouldn't be global), but their multi-mode interference patterns travel with large, often supersonic, apparent velocities over the solar surface; indeed, the 5-min curve in the lower panel does not exhibit comparable persistence. The disparity between the upper and lower panels indicates that some other agent produces partial persistence in the chromospheric three-minute oscillation amplitude patterns.

The middle panel tests whether temporal persistence is present in the K–G crosstalk peaks of Fig. 9; the latter are reproduced at $\Delta t = 0$. The 5–min crosstalk peak is higher than the 3–min peak; the crosstalk decays at similar rates for both.

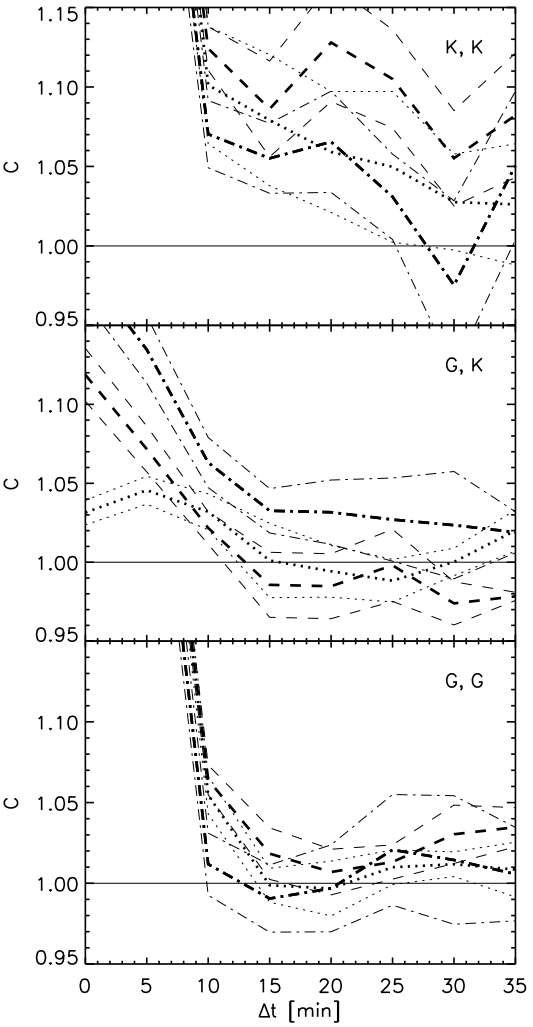

Fig. 10. Fourier persistence, measured as spatial correspondence $C(\Delta t)$ between internetwork pixels with higher than average amplitude in two Fourier amplitude maps as function of the time delay Δt between the two maps. Top panel: K maps compared with K maps. Middle panel: K maps compared with G maps, K measured after G for $\Delta t > 0$. Bottom panel: G maps compared with G maps. Dash-dotted: correspondence between successive 5-min Fourier maps. Dashed: same for 3-min maps. Dotted: same for 2-min maps. The thin curves specify rms error estimates. The spatial morphology of the G Fourier maps does not survive longer than the temporal resolution of 15 min (bottom panel), but the internetwork areas of the K Fourier maps maintain some morphology over longer duration, especially at 3-min periodicity (top panel). The middle panel indicates some preference for K areas with above-average 5-min amplitude to be located above G areas that earlier had above-average 5-min amplitude

5. Discussion

The key plots of this paper are the differential Fourier amplitude spectra in Fig. 5 and the Fourier amplitude maps in Figs. 6–7. They combine into a complex picture, mixing global and local properties for various phenomena that are not easily disentangled.

The lower panel of Fig. 5 indicates that the photospheric 5-min amplitudes are dominated by global modes without any difference between granular and intergranular locations, but that the darkest intergranular lanes possess significant localized excess of shorter-period oscillations. The overlying chromosphere (upper panel) also shows excess amplitude for intergranular features, but over the 3–7 min range and with a sudden drop around $f = 5$ mHz.

The maps in Figs. 6–7 display rich fine structure with complex topology in the form of speckled patterns with large amplitude variations, ranging from values near zero to twice the average amplitude (tracings in Fig. 6) and with a morphology split between high and low amplitude regions (Fig. 7). Although the maps describe quite different regimes, being split between photosphere (G) and chromosphere (K) as well as three intrinsically different periodicities, they display similar morphology except for the pattern scale changes. The latter increase with periodicity and with height in the atmosphere.

The spatial decompositions in Fig. 8 show that the map morphologies result from broad-band signals combining many different wavenumber components, with the scale changes corresponding to gradual shifts in the wavenumber distributions. The mix contains the granular and mesogranular scales as well as the full wavenumber range of oscillatory contributions from both global modes and locally excited waves. Thus, the morphology of the amplitude maps betrays complex combination of solar convective flows and oscillations of various sorts. Several aspects require discussion.

5.1. Data quality

Our data are affected by atmospheric seeing, limited statistics and poor response. Differential seeing motions between the G and K images may spoil our G–K co-location measurements to some extent, but the significant split between the bright granules and the dark lanes in the upper panel of Fig. 5 shows that the G–K coregistration has not been fully washed out by seeing at granular scales. The oscillation patches of which the G–K co-location is measured in the middle panel of Fig. 9 are made up from larger-scale components (Fig. 8), so that the low values of these crosstalk peaks are probably intrinsic.

Seeing jitter also produces non-solar modulation which may contribute to the high-frequency tails of the temporal spectra in Fig. 4 and the high-wavenumber tails of the spatial spectra in Fig. 8.

The smallness of the field and the limited duration of the 1.3 h image sequences limit the statistical significance of the differential amplitude and correspondence graphs. For example, we have tried to find whether the worm-like low-amplitude areas in the Fourier maps stand out in crosstalk or persistence measurements as those in Figs. 9 and 10, but the number of low-power pixels is too small for significance in such experiments. In addition, the observed field samples only about one supergranulation cell and only a few mesogranular cells. These may be atypical and not describe average solar properties properly.

Our use of G and K intensities to study oscillations is less direct than the use of Dopplershift measurements. In particular, the oscillatory modulation of the Ca II K inner-core brightness is much smaller than the corresponding modulation of K_3 line-center shift. Comparison of the middle panels of Figs. 4 and 5 of Lites et al. (1993) – or the better reproduction on page 386 of Rutten (1996) – shows that K_3 intensity modulation mimics K_3 Dopplershift modulation, though at lower response. Our K filtergram passband represents a mixture of the two H intensity panels of the latter figure, but its modulation should still represent a reasonable proxy to measure relative oscillation amplitude distributions over the solar surface. Since the spatial correspondence parameter C does not depend on the quality of the response but compares relative distribution contrasts only, our K co-location analyses should not be overly affected by the limited response of the measured brightness to oscillatory modulation.

In summary, the data used here suffer from seeing, low statistics, inadequate solar surface sampling and limited response to oscillatory modulation. The various pattern properties displayed above should therefore be treated as hints rather than facts, in need of confirmation from more extended and better-quality data sets. Nevertheless, these hints are of sufficient interest to warrant such future efforts and to be discussed in more detail below.

5.2. Wave sources

The curves in Fig. 5 indicate the presence of local wave enhancements above dark intergranular lanes, for 3 min waves in the photosphere and for 5-min waves in the chromosphere respectively. The "acoustic event" studies of Goode et al. (1992), Restaino et al. (1993), Espagnet (1994), Rimmele et al. (1995) and Espagnet et al. (1996) have also concluded that dark intergranular features tend to correlate with enhanced wave amplitudes in the photosphere. However, these studies concern 5-min waves rather than 3-min ones, whereas the statistical averages in Fig. 5 show no photospheric amplitude sensitivity to granular structure around 5-min periodicity. This difference indicates that without specific event selection the average photospheric 5-min signal is dominated by the global p-modes.

The worm-like low-amplitude areas in Fig. 7 look like node lines in a pattern of standing oscillations, suggesting that they arise from global mode interferences. However, they should then be less distinct in the 2-min map than in the 5-min map because the global contribution is much larger at the peak of the p-mode amplitudes. This is not the case; the 2-min map shows similar worm morphology as the longer-period ones. On the other hand, the worm lengths and their very low amplitude values seem to deny small-scale local wave excitation by granular or intergranular pistoning.

Neither the global nor the local agents explain the pattern scale changes between photosphere and chromosphere. Global modes should provide similar patterning to both layers, producing higher correspondence between G and K than observed. Local wave excitation at granular scales should contribute a

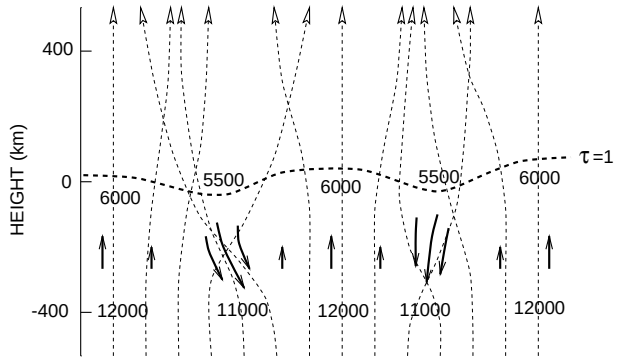

Fig. 11. Sketch illustrating how the solar granulation may affect acoustic patterning through differential diffraction of propagating waves. The vertical cut through the surface layers is patterned after Figs. 4 and 5 of Bruls & Rutten (1992). The sizable velocity and temperature gradients across granules and intergranular lanes cause divergence and convergence of upward propagating waves. Subsurface wave focusing may produce both wave concentration and wave dilution in higher layers. Similar diffraction patterns may be caused by larger-scale inhomogeneities for longer wavelengths. The sketch is for a global wave field running up from below and uses simple geometrical refraction rather than diffraction in order to supply a schematic illustration of wave bending. Additional patterning, with its own refractive confusion, may be generated by local wave sources such as breakthrough granules, supersonic granular outflows, intergranular sinks and high-speed downflow fingers in deeper layers

ubiquitous haze of chromospheric power, without the large-amplitude fluctuations at the much larger scales evident in the K panels of Fig. 7. These mesoscale wavelengths have been noticed before (e.g., Cram 1978; Damé et al. 1984; Damé & Martić 1987) but are not understood (cf. Straus et al. 1992; Straus & Bonaccini 1997). Its scale resembles the scale of the mesoscale divergence/convergence patterns measured in horizontal flows and the corresponding surface distributions of exploding granules (e.g., November et al. 1981; Simon et al. 1988; Title et al. 1989; Brandt et al. 1991; November 1994; Wang et al. 1995), for which Rast (1995) has proposed that they are set by downflow geometry through downflow driving of the convection. Since the results of Carlsson & Stein (1997) indicate that large 3-min modulation at the level of Ca II K core formation results from large 3-min modulation in the directly underlying photosphere, one may suspect that the mesoscale amplitude patterning at the chromospheric level has to do with acoustic source distributions, for example in the form of supersonic granular outflow at the surface or subsurface deep-finger patterning. However, the low value of the 3-min correspondence peak in Fig. 9 and the fact that the darkest areas in Fig. 7 display mesoscale connectivity argue against such one-to-one relationships.

5.3. Wave diffraction

Some features in our results bring us to propose yet another ingredient to the observed complexity, namely the presence of wave diffraction at various scales. Fig. 11 sketches what we mean. It depicts a schematic vertical cut through the granulation layer based on the numerical simulations of Nordlund & Stein (Stein & Nordlund 1989, Nordlund & Stein 1990). These suggest that the updrafts in the centers of granules are about 2 km s^{-1} while the downdrafts in the intergranular lanes reach 4 km s^{-1}, and that intergranular lanes are cooler than granules by about 500 K at the solar surface and by about 1500 K at a depth of 200 km. Such temperature (T) and velocity (v) fluctuations affect the phase velocity $c = \sqrt{\gamma RT/\mu} + v$ for upward propagating acoustic waves; local changes in T and v cause wave bending. The corresponding index of refraction $n = c_1/c_2$ amounts to $n \approx 0.93$ for a 1500 K temperature difference and to $n \approx 1.13$ for a 2 km s^{-1} flow difference. These values are considerable, especially for the flows. As sketched in Fig. 11, waves that propagate upward through a granule are refracted into divergence by the horizontal velocity gradient between the fast upwelling at the granule center and the slow upwelling at the edge. The larger downflow gradient across intergranular lanes causes convergence, so that intergranular lanes act as lenslets. These may produce apparent wave intensity increase, but they may also produce subsurface foci that result in beam spreading and corresponding lower intensity above the surface. We surmise that such dilution may contribute to the very low amplitude values of the extended rope-like minima in Fig. 7.

Wave diffraction may also explain other results above. The dark-lane curve in the lower panel (G data) of Fig. 5 shows considerable enhancement above $f = 4$ mHz, indicating an increasing contribution by waves that are locally excited in dark lanes or that are diffracted by the lanes into convergence at the surface. The enhanced amplitudes for 2–5 mHz of the dark-lane curve in the upper panel also indicate increased chromospheric modulation above dark lanes, with a corresponding lack of modulation above the brightest granules. This suggests that lanes generate waves that reach the chromosphere vertically or that granulation projects a focus/defocus pattern into the chromosphere. The steep drop around $f = 5$ mHz in this curve is hard to explain as a source property or as a seeing effect. It sits at the photospheric transition from evanescent to propagating waves and it may therefore imply that the latter waves have been refracted away from the lane locations by the time they reach the chromosphere. An alternative explanation may be that the lower-frequency waves have too long wavelengths to be affected at granular scales.

Another indication of wave diffraction consists of the surprisingly low values of the co-location peaks in the middle panel of Fig. 9. Global oscillations with primarily vertical wave motions should display high spatial correspondence between the photosphere and the low chromosphere, not only for the evanescent 5-min amplitudes which should show instantaneous linkage, but also for the 3-min waves which travel up much faster than the time resolution set by our sequence lengths. Waves that are locally excited underneath a plane-parallel atmosphere should also show up preferentially above the source location. Diffractional wave path bending may upset such preferential co-location.

This proposition extends the brief suggestion of Deubner & Laufer (1983) that intergranular lanes may focus 2-min waves so that these appear preferentially above lanes (as in the lower panel of Fig. 5) even if they are excited elsewhere. In the context of helioseismology, wave retardation has been mostly studied to explain mode frequency shifts (e.g., Brown 1984, Zhugzhda & Stix 1994) and mode line widths (Goldreich & Murray 1994). In local time-distance helioseismology the arrival time disturbances due to subsurface flows are sampled to map such flows in detail (e.g., Kosovichev 1996; Duvall et al. 1997).

The sketch is for refraction by solar granulation. Note that for scales comparable to the wavelength, diffraction furnishes a better description than refraction; the geometrical description used in the sketch is meant generically. Similar ray path deformations may occur when larger-scale flow patterns at larger depth affect the propagation of waves that have too long wavelengths to be diffracted by granular flows or that have sufficiently long periods to be already evanescent in the surface regime. Yet longer wavelengths may be diffracted by flows arranged in grating-like arrays with larger-scale regularity (Y.D. Zhugzdha, private communication). Thus, different scales in the convective flows may affect waves of different periodicity differently.

The largest diffraction is presumably caused by the slender high-velocity downdrafts in the subsurface convective flow patterns. Their subsurface wave focusing may produce low-amplitude regions on the surface at mesogranular scales. They would resemble the caustic light patterns projected on the bottom of a swimming pool by the variable amount of diffraction in the surface undulations. In those, the wave tops act as lenses that gather light into bright, dappled bands on the bottom. Our suggestion is that the solar subsurface flows (and to a lesser extent temperature inhomogeneities) may similarly focus and defocus waves on their way up to the surface, and that such wave concentration and dilution may contribute to the mesoscale surface amplitude patterning in Figs. 6–7.

6. Conclusions

We have introduced a technique of short-duration Fourier mapping at high spatial resolution to correlate co-location of dynamical phenomena in the solar atmosphere statistically. The technique has been used here to study the morphology of acoustic amplitude distributions obtained from the brightness modulation of cospatial G-band and Ca II K filtergram sequences.

We have found that global and local wave properties combine into a mix of small-scale wave patterning with large multi-agent complexity. The latter justifies our statistical approach. The photospheric 3-min patterns show a significant contribution from intergranular lanes while the photospheric 5-min patterning in our maps is dominated by global p-modes. The mesoscale patterning of the chromospheric wave modes sampled by Ca II K intensity remains a puzzle. Our suspicion is that this pattern derives indirectly from wave source distributions that are set by convective flows. The extended worm-like connectivity of the low-amplitude areas in Fig. 7 may represent mapping artifacts – not unlike Mars channels – but we speculate that their large extent and their mesoscale patterning have to do with subsurface source topology and that their low amplitudes have to do with subsurface wave diffraction.

The apparent temporal persistence of this pattern (Fig. 10) is studied in the next paper in this series (Hoekzema & Rutten 1997), where the same techniques are used on the same data in order to study time-delayed co-location of photospheric and chromospheric waves and fine structure elements in more detail.

Acknowledgements. We are grateful to Göran Scharmer for permission to use the SVST, Rolf Kever, Göran Hosinsky and Paco Armas for assistance at the telescope and Zoe Frank and the late Kermit Smith for help with the data reduction at the Lockheed Palo Alto Research Laboratories. Javier Trujillo Bueno took part in the observing campaign. N.M. Hoekzema's research was supported by the Netherlands Foundation for Research in Astronomy (NFRA) with financial aid from the Netherlands Organization for Scientific Research (NWO). P.N. Brandt and R.J. Rutten acknowledge travel support from NATO (CRG nr. 900229) and much hospitality at Lockheed.

References

Berger T. E., Title A. M. 1996, ApJ, 463, 365
Berger T. E., Schrijver C. J., Shine R. A., Tarbell T. D., Title A. M., Scharmer G. 1995, ApJ, 454, 531
Brandt P. N., Ferguson S., Scharmer G. B. et al. 1991, A&A, 241, 219
Brandt P. N., Rutten R. J., Shine R. A., Trujillo Bueno J. 1992, in M. S. Giampapa, J. A. Bookbinder (eds.), Cool Stars, Stellar Systems, and the Sun, Proc. Seventh Cambridge Workshop, Astron. Soc. Pac. Conf. Series 26, p. 161
Brandt P. N., Rutten R. J., Shine R. A., Trujillo Bueno J. 1994, in R. J. Rutten, C. J. Schrijver (eds.), Solar Surface Magnetism, NATO ASI Series C 433, Kluwer, Dordrecht, p. 251
Brown T. M. 1984, Science, 226, 687
Brown T. M. 1991, ApJ, 371, 396
Brown T. M., Bogdan T. J., Lites B. W., Thomas J. H. 1992, ApJ, 394, L65
Bruls J. H. M. J., Rutten R. J. 1992, A&A, 265, 257
Carlsson M., Stein R. F. 1994, in M. Carlsson (ed.), Chromospheric Dynamics, Proc. Miniworkshop, Inst. Theor. Astrophys., Oslo, p. 47
Carlsson M., Stein R. F. 1997, ApJ, 481, 500
Cattaneo F., Hurlburt N. E., Toomre J. 1989, in R. J. Rutten, G. Severino (eds.), Solar and Stellar Granulation, NATO ASI Series C 263, Kluwer, Dordrecht, p. 415
Cattaneo F., Hurlburt N., Toomre J. 1990, ApJ, 349, L63
Cheng Q.-Q., Yi Z. 1996, A&A, 313, 971
Cram L. E. 1974, Solar Phys., 37, 75
Cram L. E. 1978, A&A, 70, 345
Cram L. E., Damé L. 1983, ApJ, 272, 355
Cram L. E., Brown D. R., Beckers J. M. 1977, A&A, 57, 211
Damé L., Martić M. 1987, ApJ, 314, L15
Damé L., Gouttebroze P., Malherbe J.-M. 1984, A&A, 130, 331
Deubner F.-L. 1975, Solar Phys., 40, 333
Deubner F.-L., Fleck B. 1989, A&A, 213, 423
Deubner F. L., Laufer J. 1983, Solar Phys., 82, 151
Duvall T. L., Kosovichev A. G., Scherrer P. H. et al. 1997, Solar Phys., 170, 63
Endler F., Deubner F. L. 1983, A&A, 121, 291

Espagnet O. 1994, La granulation solaire: origine, pénétration dans la photosphère et interactions avec les oscillations de 5 minutes, Thesis Université Paul Sabatier, Toulouse
Espagnet O., Muller R., Roudier T. et al. 1996, A&A, 313, 297
Evans J. W., Michard R. 1962, ApJ, 136, 493
Goldreich P., Keeley D. A. 1977, ApJ, 212, 243
Goldreich P., Kumar P. 1990, ApJ, 363, 694
Goldreich P., Murray N. 1994, ApJ, 424, 480
Goode P. R., Gough D., Kosovichev A. G. 1992, ApJ, 387, 707
Harvey J. 1977, Highlights of Astronomy, 4 Part II, 223
Hoekzema N. M., Rutten R. J. 1997, A&A, in press
Hofmann J., Steffens S., Deubner F. L. 1996, A&A, 308, 192
Kalkofen W. 1996, ApJ, 468, L69
Keller C. U., Deubner F. L., Egger U., Fleck B., Povel H. P. 1994, A&A, 286, 626
Kosovichev A. G. 1996, ApJ, 461, L55
Kulaczewski J. 1992, A&A, 261, 602
Kumar P. 1994, ApJ, 428, 827
Lighthill M. J. 1952, Proc. R. Soc. Lond. A, 211, 564
Lin H. 1995, ApJ, 446, 421
Lites B. W., Leka K. D., Skumanich A., Martinez Pillet V., Shimizu T. 1996, ApJ, 460, 1019
Lites B. W., Rutten R. J., Kalkofen W. 1993, ApJ, 414, 345
Liu S.-Y. 1974, ApJ, 189, 359
Liu S. Y., Sheeley N. R. 1971, Solar Phys., 20, 282
Livingston W., Harvey J. 1971, in R. Howard (ed.), Solar Magnetic Fields, IAU Symposium 43, Reidel, Dordrecht, p. 51
Malagoli A., Cattaneo F., Brummell N. H. 1990, ApJ, 361, L33
Meyer F., Schmidt H. U. 1967, Zeitschr. f. Astrophys., 65, 274
Muller R., Hulot J. C., Roudier T. 1989, Solar Phys., 119, 229
Muller R., Roudier T. 1992, Solar Phys., 141, 27
Musielak Z. E., Rosner R., Stein R. F., Ulmschneider P. 1994, ApJ, 423, 474
Musman S., Rust D. M. 1970, Solar Phys., 13, 261
Nesis A., Bogdan T. J., Cattaneo F. et al. 1992, ApJ, 399, L99
Nordlund Å., Stein R. F. 1990, Comp. Phys. Comm., 59, 119
November L. J. 1994, Solar Phys., 154, 1
November L. J., Toomre J., Gebbie K. B., Simon G. W. 1981, ApJ, 245, L123
Noyes R. W. 1967, in R. N. Thomas (ed.), Aerodynamic Phenomena in Stellar Atmospheres, IAU Symp. 28, Academic Press, London, p. 293
Orrall F. Q. 1966, ApJ, 143, 917
Owocki S. P., Auer L. H. 1980, ApJ, 241, 448
Rast M. P. 1995, ApJ, 443, 863
Restaino S. R., Stebbins R. T., Goode P. R. 1993, ApJ, 408, L57
Rice E., Gaizauskas V. 1973, Solar Phys., 32, 421
Rimmele T. R., Goode P. R., Harold E., Stebbins R. T. 1995, ApJ, 444, L119
Roudier T., Malherbe J. M., November L. et al. 1997, A&A, 320, 605
Rutten R. J. 1994, in M. Carlsson (ed.), Chromospheric Dynamics, Proc. Miniworkshop, Inst. Theor. Astrophys., Oslo, p. 25
Rutten R. J. 1995, in J. T. Hoeksema, V. Domingo, B. Fleck, B. Battrick (eds.), Helioseismology, Proc. Fourth SOHO Workshop, ESA SP–376 Vol. 1, ESA Publ. Div., ESTEC, Noordwijk, p. 151
Rutten R. J. 1996, in K. G. Strassmeier, J. L. Linsky (eds.), Stellar Surface Structure, Procs. Symp. 176 IAU, Kluwer, Dordrecht, p. 385
Rutten R. J., Uitenbroek H. 1991, Solar Phys., 134, 15
Scharmer G., Brown D., Petterson L., Rehn J. 1985, Appl. Opt., 24, 2558
Simon G. W., Title A. M., Topka K. P. et al. 1988, ApJ, 327, 964
Solanki S. K., Rueedi I., Bianda M., Steffen M. 1996, A&A, 308, 623
Steffens S., Deubner F.-L., Hofmann J., Fleck B. 1995, A&A, 302, 277
Stein R. F. 1967, Solar Phys., 2, 285
Stein R. F., Nordlund Å. 1989, ApJ, 342, L95
Stix M. 1970, A&A, 4, 189
Straus T., Bonaccini D. 1997, A&A, in press
Straus T., Deubner F.-L., Fleck B. 1992, A&A, 256, 652
Strous L. H. 1994, Dynamics in Solar Active Regions: Patterns in Magnetic-Flux Emergence, PhD Thesis, Utrecht University
Theurer J., Ulmschneider P., Cuntz M. 1997, A&A, in press
Title A. M., Berger T. E. 1996, ApJ, 463, 797
Title A. M., Tarbell T. D., Topka K. P., Ferguson S. H., Shine R. A., the SOUP Team 1989, ApJ, 336, 475
Title A. M., Topka K. P., Tarbell T. D. et al. 1992, ApJ, 393, 782
von Uexküll M., Kneer F. 1995, A&A, 294, 252
Wang J., Wang H., Tang F., Lee J. W., Zirin H. 1995, Solar Phys., 160, 277
Wang Y., Noyes R. W., Tarbell T. D., Title A. M. 1995, ApJ, 447, 419
Wang H., Tang F., Zirin H., Wang J. 1996, Solar Phys., 165, 223
Zhugzhda Y. D., Stix M. 1994, A&A, 291, 310
Zwaan C. 1987, ARA&A, 25, 83

This article was processed by the author using Springer-Verlag LaTeX A&A style file *L-AA* version 3.